



## Image-based calibration of rolling resistance in discrete element models of sand

R. Rorato <sup>a,\*</sup>, M. Arroyo <sup>a</sup>, A. Gens <sup>a</sup>, E. Andò <sup>b</sup>, G. Viggiani <sup>b</sup>

<sup>a</sup> Department of Civil and Environmental Engineering, Universitat Politècnica de Catalunya (UPC), Barcelona, Spain

<sup>b</sup> Univ. Grenoble Alpes, CNRS, Grenoble INP, 3SR, F-38000 Grenoble, France



### ARTICLE INFO

#### Keywords:

Discrete element method  
Rolling resistance  
Particle shape  
X-rays micro tomography  
Triaxial test  
Shear resistance

### ABSTRACT

Models that introduce rolling resistance at the contact are widely employed in simulations using the discrete element method (DEM) to indirectly represent particle shape effects. This approach offers substantial computational benefits at the price of increased calibration complexity. This work proposes a method to simplify calibration of rolling resistance. The key element is an empirical relation between a contact parameter (*rolling friction*) and a 3D grain shape descriptor (*true sphericity*). Values of true sphericity can be obtained by image analysis of the grains, either directly by 3D acquisition or by correlation with simpler-to-obtain 2D shape measures. Evaluation of rolling friction is thus made independent from that of other model parameters. As an extra benefit, the variability of grain shape in natural sands can be directly mapped into the discrete model. A mapping between rolling friction and true sphericity is calibrated using specimen-scale and grain scale results from two triaxial compression tests on Hostun sand and Caicos ooids. The mapping is validated using different triaxial tests from the same sands and from other reference sands (Ottawa, Ticino). In the case of Ticino grain-shape acquisition is made in 2D, using an ordinary table scanner. The results obtained support this direct calibration procedure.

### 1. Introduction

Powered by increased computational performance, the discrete element method (DEM) has gained much relevance in geomechanics since originally proposed by Cundall and Strack (1979). DEM models at specimen scale are now a basic tool of research to study and illuminate many features of soil mechanics observed in the laboratory (Giantia et al., 2019a; Li et al., 2018; Hosn et al., 2018). There is also a growing trend to use DEM models to analyse large scale problems of direct engineering relevance (Zhang et al., 2019; Zhang and Evans, 2019; Butlanska et al., 2018; Kawano et al., 2018). As in other numerical modelling approaches, there is always an underlying conflict between model resolution and computational efficiency. This tension is particularly vivid in the consideration of particle shapes in DEM.

The most widely used shape in 3D DEM is the sphere (as is the disk in 2D DEM). The reason is pragmatic: spheres allow straightforward and computationally efficient contact detection, which is a large part of the computational cost of every step. Unfortunately soil particles are not generally spherical but have instead very varied shapes. In coarse soils,

research has clearly identified large particle shape effects for several important properties such as extreme void ratios (Cho et al., 2006), critical state friction (Yang and Luo, 2015) or dilatancy and peak friction (Xiao et al., 2019). Particle shape also affects responses of major engineering significance, like liquefaction resistance (Vaid et al., 1985) or cone tip resistance (Liu and Lehane, 2013).

Direct experimental evidence for the role of shape in soils was reinforced by DEM models in which grain shape was directly controlled. For instance, just switching from disks to ellipses (Rothenburg and Bathurst, 1992) or from spheres to ellipsoids (Lin and Ng, 1997) raised numerical shear strength and dilatancy values to within the range observed in soils.

Ellipses and ellipsoids are still far from the shapes observed in most soil particles. Several techniques have been developed to incorporate more realism into element shapes: they use clumps or aggregates of spheres (Matsushima, 2002; Lu and McDowell, 2007; Katagiri et al., 2010); polyhedrons (Zhao et al., 2006; Boon et al., 2012); superquadrics (Williams and Pentland, 1992; Zhao et al., 2018) or level sets (Jerves et al., 2016; Kawamoto et al., 2018). Increased morphological realism

\* Corresponding author.

E-mail addresses: [riccardo.rorato@upc.edu](mailto:riccardo.rorato@upc.edu) (R. Rorato), [marcos.arroyo@upc.edu](mailto:marcos.arroyo@upc.edu) (M. Arroyo), [antonio.gens@upc.edu](mailto:antonio.gens@upc.edu) (A. Gens), [edward.ando@3sr-grenoble.fr](mailto:edward.ando@3sr-grenoble.fr) (E. Andò), [cino.viggiani@3sr-grenoble.fr](mailto:cino.viggiani@3sr-grenoble.fr) (G. Viggiani).

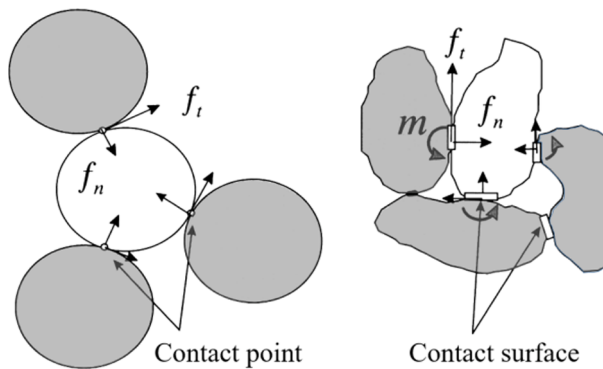


Fig. 1. Origin of rolling resistance at contact (Iwashita and Oda, 1998).

has advantages and disadvantages. One advantage is that it may be thus possible to represent the non-negligible variability in shape that is observed in granular soils. A significant disadvantage is added computational cost. Indeed, for the same problem dimensions, orders of magnitude increases in computational time with respect to sphere-based models are typically reported (Lu et al., 2015; Irazabal et al., 2017).

The micromechanics underlying the effect of element shape on shear strength was clarified by Bardet (1994), who noted that disks showed a high concentration of rotations in shear bands and that, if rotation was blocked, realistic values of friction and dilatancy ensued. Based on this and similar observations, several researchers (Sakaguchi et al., 1993, Iwashita and Oda, 1998, Jiang et al., 2005; Mohamed and Gutierrez, 2010) proposed the introduction of a resisting moment (*i.e.*, *rolling resistance*) at particle contacts (see Fig. 1). The moment applied is typically dependent on relative particle rotation, opposing it through an elasto-plastic mechanism analogous to that acting for contact forces. Sometimes a viscous component is also added to the contact formulation (see Ai et al., 2011, for a review).

Several DEM studies (Zhou et al., 2013, Wensrich et al., 2014) have compared the results obtained using aggregates of particles (*i.e.*, clumps) or adding rotational constrains, showing that both approaches result in very similar behaviour, at least for the quasi-static conditions relevant in most soil mechanics problems. The main advantage of the rolling resistance model is that contact detection remains efficient; the calibration of contact properties is, however, far from trivial.

The majority of the previous studies (Iwashita and Oda, 1998, 2000, Jiang et al., 2005, Belheine et al., 2009, Zhou et al., 2013) calibrate

rolling resistance through an empirical macroscopic approach. Specimen-scale responses of “identical” numerical and experimental test are matched by trial-and-error. The process is difficult because the effects of rolling resistance in macro-response are coupled with those of other parameters (the coefficient of sliding friction in particular), and multiple solutions are possible to match key experimental results, such as dilatancy or peak mobilised friction (Estrada et al., 2008, Wensrich and Katterfeld, 2012, Cheng et al., 2017). Calibration can thus become a very time consuming and somewhat subjective process. Alternatives based on statistically driven semi-automated calibration have been proposed, (Cheng et al., 2018) but they appear computationally intensive.

Some researchers (Calvetti et al., 2003, Arroyo et al., 2011, Ciantia et al., 2015) have simplified radically the calibration process by directly assuming very large values of moment resistance and stiffness, so as to inhibit relative rotation at the contact. This assumption does not limit the ability of the resulting discrete model to match and predict large-scale soil responses, but it does lack some subtlety.

A different approach to simplify the calibration problem would be to give some specific physical base to rolling resistance. Little work has been done to explore this possibility. Wensrich and Katterfeld (2012) proposed a definition of average contact particle eccentricity as such basis. Rorato et al. (2018) suggested instead that a physical measure of grain shape such as sphericity would offer a good basis to calibrate rolling resistance. Herein, this latter idea is developed in detail and tested with several sands.

## 2. Methodology

### 2.1. Contact rolling resistance model

This work is based on the Iwashita and Oda contact model (1998) as implemented in the commercial DEM software PFC3D V5 (Itasca Consulting Group Inc., 2014), which has been used for all the simulations presented here. The model is schematically illustrated in Fig. 2a, it includes a conventional linear elastic – frictional contact model for particle relative displacement at the contact plus an additional set of elastic spring no-tensional joint and slider for the rolling motion.

The contact normal and shear stiffness are defined as

$$k_n = \frac{AE_{mod}}{L}; k_s = \frac{k_n}{k_{ratio}} \quad (1)$$

where  $E_{mod}$  and  $k_{ratio}$  are material parameters to be calibrated,  $A$  is the

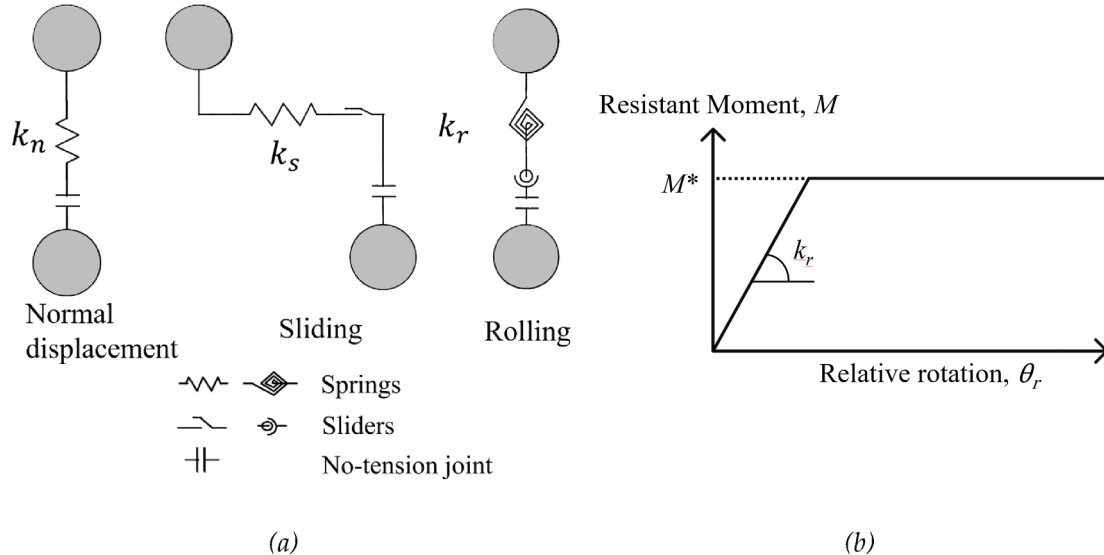


Fig. 2. Rolling resistance contact model (a) and elastic-perfectly plastic model accounting for rolling resistance at contact (b).

diameter of the smallest contacting sphere and  $L$  is the distance between grain centres. This formulation guarantees scale-invariance of the interaction law (Feng and Owen, 2014).

For the moment rotation law (Fig. 2b) the following assumptions are used

- (1). The *rolling stiffness* ( $k_r$ ) is defined as:

$$k_r = k_s R^2 \quad (2)$$

where  $k_s$  is the contact *shear stiffness* and  $R$  the *effective radius* defined as

$$R = \frac{1}{R_1} + \frac{1}{R_2} \quad (3)$$

with  $R_1$  and  $R_2$  being the radii of the two particles in contact. The proportionality of rolling and shear stiffness was derived by Iwashita and Oda (1998) to make identical the elastic moment due to shear and that due to rotation. Wensrich and Katterfeld (2012) compared this formulation of rolling stiffness with available alternatives and noted that the Iwashita-Oda approach has some numerical advantages as (a) it dampens elastic oscillations without the need to introduce extra parameters and (b) simplifies the computation of critical time steps.

- (2). The moment-rotational contact law is implemented as an elastic-perfectly plastic model with the yielding moment ( $M^*$ ) defined as:

$$M^* = \mu_r F_n R \quad (4)$$

where  $\mu_r$  is defined as *rolling friction coefficient* and  $F_n$  is the normal contact force. The rolling resistance part of the contact model used in this study is illustrated in Fig. 2b.

The Iwashita and Oda (1998) original formulation also includes viscous dissipation at the contact. Wensrich and Katterfeld (2012) showed that the effect of rotational contact viscosity on simulation outcomes is negligible for the quasi-static conditions with low inertial numbers which are of interest here. Therefore, viscous dissipation at the contact was not included in the models for simplicity.

## 2.2. Shape description

The *degree of true sphericity*,  $\psi$  (Wadell, 1932) is employed to describe grain shape.  $\psi$  is defined as

$$\psi = \frac{s_n}{S} = \frac{\sqrt[3]{36\pi V^2}}{S} \quad (5)$$

where ( $S$ ) is the particle surface area and ( $s_n$ ) is the surface area of a sphere with the same volume ( $V$ ) as the particle. As argued by Rorato et al. (2019a),  $\psi$  offers a compact, easy to interpret, and conceptually sound measure of how similar a given particle is to a sphere.

Despite its conceptual simplicity, this shape descriptor had seen relatively little use because measuring the surface area of irregular sand grains is difficult. This has changed in recent years, as computer-based 3D image analysis techniques made such measurements possible. Still, access to 3D imaging equipment is sometimes limited, and 2D images are much easier to acquire and process. For this reason a number of 2D proxy measures of sphericity have been proposed over the years (Rorato et al., 2019a). In this work we use *2D perimeter sphericity*  $S_p$ .  $S_p$  which is defined as the ratio of the perimeter of the circle with area equal to that projected by the particle to the perimeter of the actual particle projection. Note that we use oriented particle projection – i.e., the projection is made against the plane of maximum particle stability.

## 2.3. Relating rolling resistance and particle shape

Rorato et al. (2018) hypothesized that the *degree of true sphericity*

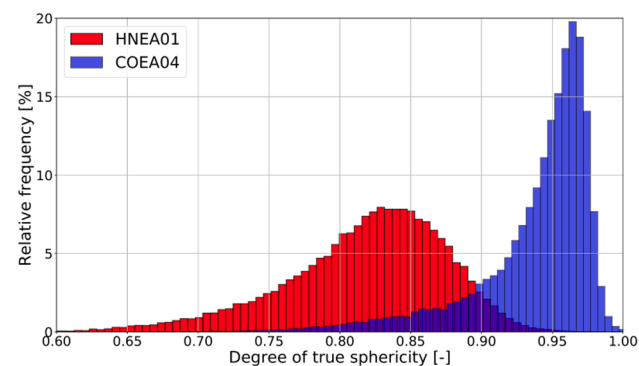


Fig. 3. Statistical distribution of the degree of true sphericity of Caicos (COEA04) and Hostun (HNEA01) sands (Rorato et al., 2019a).

may be univocally related with a *coefficient of rolling friction*, through a relation such as

$$\mu_r = F(\psi) \quad (6)$$

This kind of relation maps a physical measured sand property into a discrete element property. Such mapping may be made just on the average value of sphericity, to obtain a single value of rolling resistance to apply for all particles in a DEM model of such sand. However, when an experimental distribution of  $\psi$  such as those in Fig. 3 is available, the process can be also made element by element, assigning to each one a sampled value from the measured distribution of  $\psi$  and then applying the mapping function to initialize its rolling friction coefficient. In this way, the variability in grain shape distribution is directly reflected in the numerical model through a distribution of particle *rolling friction coefficient*.

Because rolling friction is a contact property, an extra rule is necessary to assign rolling resistance to a contact between two particles. The solution to avoid this ambiguity is to select the minimum, as

$$\mu_r = \min(\mu_{r,1}, \mu_{r,2}) \quad (7)$$

where  $\mu_{r,1}$  and  $\mu_{r,2}$  are the rolling friction coefficients of the two contacting spheres. This is the same rule that the PFC code applies to the sliding friction coefficient when two bodies of different materials contact. Thus, the rolling resisting yielding moment ( $M^*$ ) varies at each contact depending on (1) the radii of the contacting spheres, that is the *effective radius*,  $R$ , (2) the normal contact force  $F_n$  and (3) the *coefficient of rolling friction*, different for each contact (from Eqs. (6) and (7)).

## 3. Model calibration

### 3.1. Target experimental data

Two natural sands with very different particle shape were selected

Table 1

Physical properties of the different sands used for calibration and/or validation [ $D_{50}$  = mean grain size,  $C_u$  = Coefficient of uniformity,  $C_c$  = Coefficient of curvature,  $G_S$  = Specific gravity,  $e_{min}/e_{max}$  = Minimum/maximum void ratio]. Data for Hostun from (Combe, 1998), data for Caicos from (Andò, 2013), data for Ottawa from (Lee et al., 2007), data for Ticino from (Jamiolkowski et al., 2003). \* = typical value for carbonate sands.

	$D_{50}$	$C_u$	$C_c$	$G_S$	$e_{min}$	$e_{max}$	Mineralogy
Hostun	338 $\mu m$	1.41	0.95	2.65	0.605	0.927	Quartz
Caicos	420 $\mu m$	1.39	1.09	2.80*	–	–	Aragonite (96%) Calcite (3%)
Ottawa	310 $\mu m$	1.31	0.95	2.65	0.499	0.850	Quartz
Ticino	540 $\mu m$	1.60	2.32	2.68	0.582	0.934	Feldspar (65%) Quartz (30%)

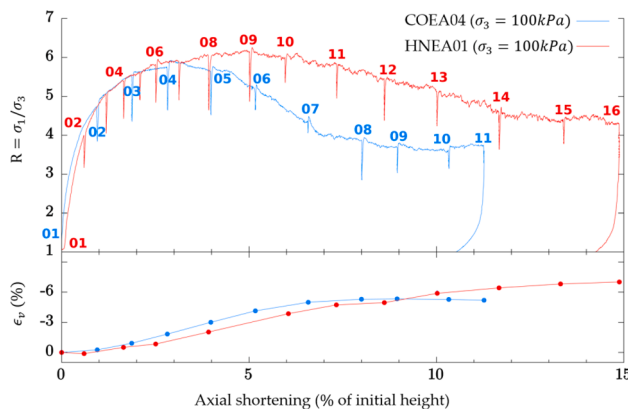


**Fig. 4.** Triaxial stress-volumetric-strain responses of Hostun sand (specimen HNEA01) and Caicos sand (specimen COEA04).

for calibration: Hostun sand, very angular, and Caicos ooids, very spherical (see Table 1, where physical properties for these sands are reported alongside those of sands later used in validation). A triaxial test campaign on various specimens of Hostun sand and Caicos ooids was performed by Andò (Andò, 2013) at Laboratoire 3SR (Grenoble). Systematic tomographic acquisition was carried out throughout. Two tests on dense Hostun sand (specimen "HNEA01") and Caicos ooids (specimen "COEA04") under 100 kPa confining pressure were selected for the calibration. The macroscopic stress strain and volumetric responses recorded in these tests are shown in Fig. 4.

Rorato et al. (2019a) examined the tomographic images of the Hostun HNEA01 and Caicos COEA04 specimens to acquire three-dimensional shape properties (e.g., volume, surface area, lengths, etc.) of every grain. One of the results thus obtained were statistical distributions of  $\psi$  for Hostun and Caicos sands (Fig. 3). Another important finding from that work was that, in the Hostun and Caicos grains, 3D true sphericity ( $\psi$ ) showed good linear correlation with the much easier to measure 2D perimeter sphericity  $S_p$ . The correlation obtained is given by

$$\psi = 1.075(S_p) - 0.067 \quad (8)$$

A different set of analyses of the scanning data from these two specimens was made to obtain a database of grain motions. In that work (see Rorato et al., 2020; Rorato, 2019b) Discrete Digital Volume Correlation (D-DVC, see Hall et al., 2010) is used to obtain the kinematical history of each sand grain in these triaxial specimens. Averaging that grain scale result for a selection of grains it is possible to obtain the average grain kinematics in a particular zone of the specimen. Because the specimens failed in a localized shear mode, there was interest in separating the behaviour inside and outside the shear bands. To individuate the grains belonging to the shear band, a nominal strain (called

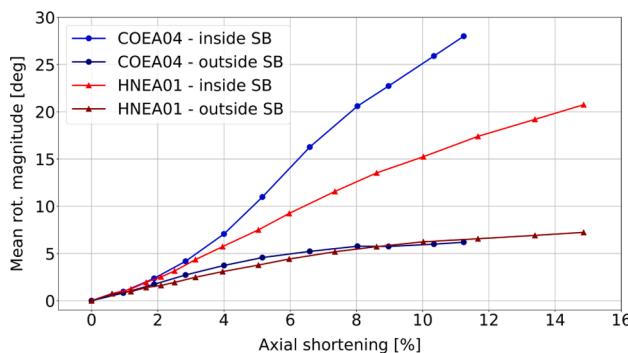


**Fig. 5.** Average cumulative rotation of sand grains inside and outside the shear band (Rorato, 2019b).

"micro-strain") was assigned to each grain. That was done – following Catalano et al. (2014) – by means of a Voronoi-based allocation of spatial domains centred around each particle. Once micro-strains are computed, a threshold shear strain value (0.1 in this study) is used to separate the particles that belong to the shear band from those that are outside of it. As a result of this work the average cumulative rotation for the grains in these specimens can be plotted (Fig. 5).

A further result from that previous work of interest here involves correlations between individual grain shape descriptors and grain rotations. The study (Rorato et al., 2020; Rorato, 2019b) showed that  $\psi$  is one of the shape descriptors that best correlated with cumulative grain rotation, particularly for grains that are inside the shear bands.

### 3.2. Mapping function

A monotonically increasing mapping function,  $F(\psi)$ , seems reasonable, as it provides low values of rolling friction when grain sphericity is high, and vice-versa. Rolling friction values used in previous studies usually range between 0 and 1, although some researchers (e.g., Hosn et al., 2018) have explored higher values. True sphericity  $\psi$  has a relatively narrow range in practice. A cube, for instance, has a value of  $\psi = 0.81$ ; detailed examination shows that grain  $\psi$  values below 0.6 in Fig. 3 likely result from image segmentation errors (Rorato et al., 2019a).

In a first approximation it may seem tempting to assume a zero value of  $\mu_r$  for a sphere ( $\psi = 1$ ). However, such assumption has a serious limitation, as the rolling resistance of spherical particles may be significant due to mechanisms such as contact deformation (Jiang et al., 2005) and/or surface interlocking due to contact roughness (Huang et al., 2017). It is thus preferable to allow for a finite value of  $\mu_r$  at the upper limit of sphericity. The mapping function selected for calibration takes then an exponential form

$$\mu_r = A(\psi)^{-b} \quad (9)$$

### 3.3. Calibration procedure

The parameters of the contact model available for fitting are thus  $E_{mod}$ ,  $k_{ratio}$  and contact sliding friction  $\mu$ . Apart from that, the two parameters of the sphericity to rolling resistance mapping function,  $A$  and  $b$  also require calibration.

This set of parameters was calibrated, by trial and error, to adjust not only the specimen scale macroscopic response illustrated in Fig. 4, but also the observed evolution of average rotation within the shear bands reported in Fig. 5. This rotation evolution was included as the macroscopic stress-strain information does not offer enough information on the particle rolling behaviour that is directly related to rotational resistance in DEM. In principle, the contact model parameters may be different for each sand, as they are presumed to reflect grain properties not explicitly accounted for in the model, such as mineralogy or roughness. On the other hand, the sphericity-rolling resistance mapping function parameters are presumed to be unique for all sands as the function already incorporates the effect of different sand grain shapes.

DEM cylindrical specimens were prepared to be tested in triaxial compression. The specimens matched the particle size distribution (PSD) of the actual specimens. The small size of the tested specimens (10 mm diameter and 20 mm height) made scaling unnecessary, and the numerical specimens maintained the same scale as the experiments. Doing so, the initial models contain about 60.000 particles, close to the number of sand grains identified inside specimens HNEA01 and COEA04. To attain prescribed initial conditions of density and pressure arbitrarily low initial friction coefficients ( $\mu_0$ ) were used to facilitate specimen formation after seeding. The specimens were then isotropically compressed up to 100 kPa.

The DEM specimens were limited by a cylindrical wall element on the outer periphery and two horizontal walls at the top and bottom. The radius of the horizontal wall was servo controlled during loading to

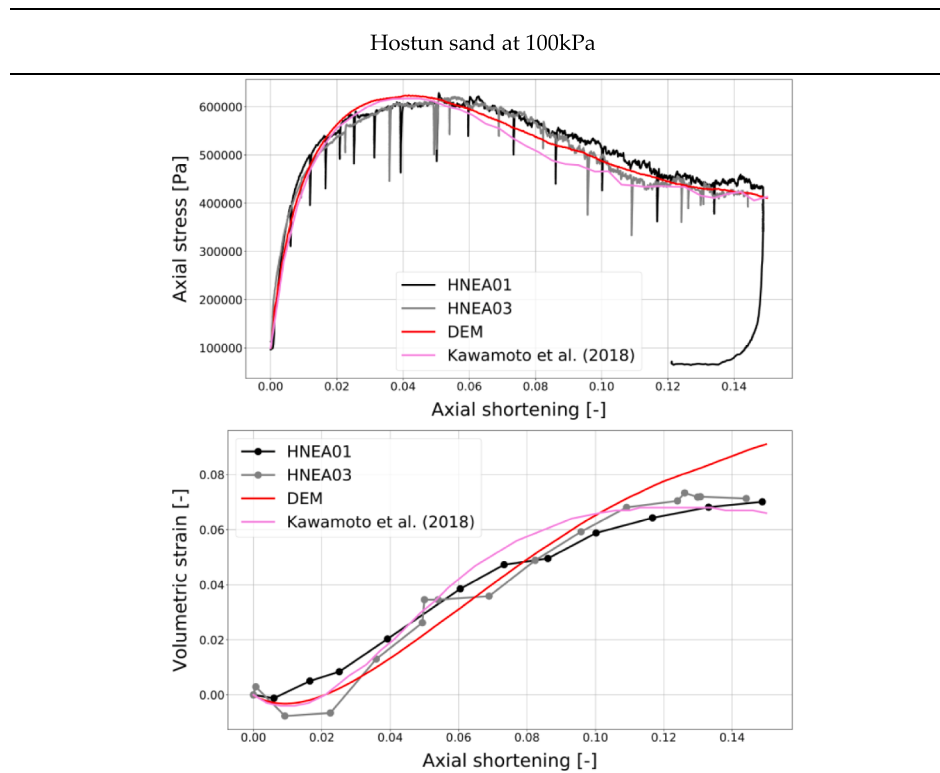


**Fig. 6.** Comparison between the triaxial responses (100 kPa confining pressure) of the experiments (specimens HNEA01 and HNEA03) and the numerical model (DEM) replicating Hostun sand.

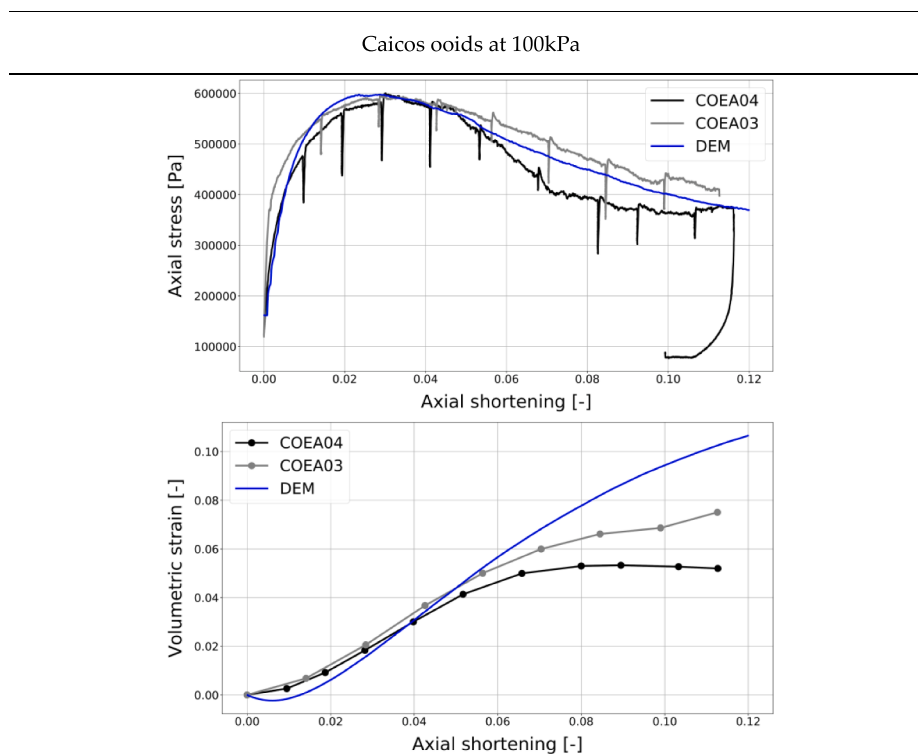


**Fig. 7.** Comparison between the triaxial responses (100 kPa confining pressure) of the experiments (specimens COEA03 and COEA04) and the numerical model (DEM) replicating Caicos ooids.

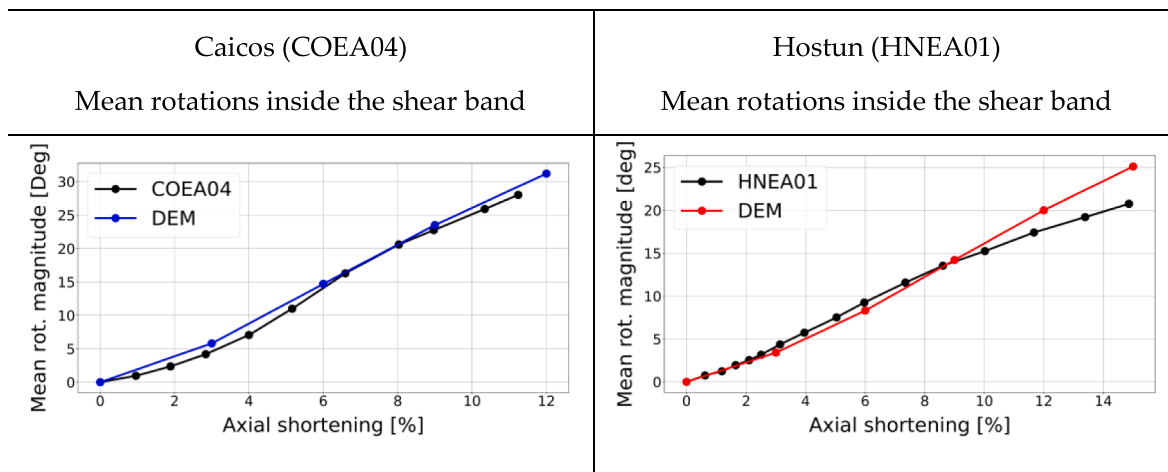


**Fig. 8.** Mean particle rotations for the grains located inside the shear bands (the black grains of Fig. 10) for both the experimental and numerical samples, throughout the execution of the triaxial test. The good fit ensures the kinematics at failure is respected.

maintain a constant pressure. During shearing a constant vertical velocity is applied to the top and bottom walls; this velocity was selected to maintain a low inertial number,  $I$ , which is defined as (Da Cruz et al., 2005):

$$I = \frac{\dot{\gamma}D_{50}}{\sqrt{P/\rho}} \quad (10)$$

where  $\dot{\gamma}$  is the shearing rate,  $P$  is the pressure level (confining pressure) and  $\rho$  is the particles density.

The same Voronoi-cell based procedure (Catalano et al., 2014) employed to assign microstrain to grains in the experimental specimens was also applied to the numerical specimens. Grains belonging to a shear band were identified by the assigned shear strain value attained towards the end of the test. The same microstrain shear threshold value used to analyse the experiments (0.1) was also applied here. For all elements assigned to the shear band, their kinematic history was then analysed to extract individual particle rotations, which were then averaged to compare with the equivalent experimental data.

The trial and error parameter calibration procedure followed well established heuristics for the linear elasto-plastic model (Butlanska, 2014), with parameter  $E_{mod}$  mostly selected to match initial stiffness,  $k_{ratio}$  to match initial dilatancy and  $\mu$  to match peak strength. The mapping function parameters were mostly adjusted to match the average rotation vs strain curves, although they also affected post-peak stress-strain behaviour. After a few rounds of iterations, the responses illustrated in Fig. 6, Fig. 7 and Fig. 8 were considered to offer a satisfactory match to the experiments. These results were obtained using the parameters reported in Table 2 -where the parameters of other sands used in later validation simulations are also included.

Somewhat surprisingly, the adjusted values of the sliding friction coefficients (0.575) and the stiffness parameters (effective normal stiffness, stiffness ratio) were identical for both sands. The parameters fitted for the mapping function result in

$$\mu_r = 0.1963(\psi)^{-8.982} \quad (11)$$

and this power function is plotted in Fig. 9. The calibration result assigns a minimum limiting rolling friction coefficient of about 0.2 to perfectly spherical particles ( $\psi = 1$ ).

The match obtained for the axial stress-strain behaviour is rather good. Figs. 6 and 7 also include results from two experimental replicas of the tests used in calibration, test HNEA03 for Hostun and test COEA03 for Caicos. It can be seen that the numerical results fit well within the baseline experimental variability given by the test replicas.

A slight discrepancy is noted in the volumetric vs. axial strain curves.

The numerical specimens keep on dilating towards the end when the experimental curves are becoming flat. This is most likely an effect of the simplified model used to represent the cylindrical membrane employed in the physical experiments. The servo controlled external rigid wall employed in the numerical model forces a uniform radial expansion of the specimen, that is particularly unrealistic after shear localization takes place. This effect of radial rigid walls on apparent (post localization) dilatancy was recently demonstrated by Khoubany and Evans (2018).

Fig. 8 shows that an excellent match was attained for the mean particle rotation history inside the shear bands. The overall aspect of the shear bands identified in the numerical simulations is compared with the experimental results in Fig. 10. The numerical sample is clearly able to localise the strain, although due to the rigid radial boundary condition applied, the bands are thicker and extend further to the corners. However, the fact that the shear band of Hostun is thicker than that of Caicos (due to increased interlocking effects) indicates that shear band thickness variation is qualitatively reproduced in these DEM simulations.

**Table 2**  
Parameters and input variables employed in the DEM simulations.

Parameter	Symbol	Hostun	Caicos	Ottawa	Ticino
Specimen sizes (height, diameter)	$H_c(\text{mm})$ $D_c(\text{mm})$	20 10	20 10	20 10	20 10
Effective normal contact stiffness	$E_{mod}(10^8 \text{Pa})$	2.0	2.0	1.5	4.0
Normal-to-shear stiffness ratio	$k_{ratio}$	2.0	2.0	2.0	2.0
Inter-particle friction coefficient	$\mu$	0.575	0.575	0.450	0.600
Degree of true sphericity	$\psi$	(Fig. 13)	(Fig. 13)	(Fig. 13)	(Eq. (8))
Rolling friction coefficients	$\mu_r$	(Eq. (11))	(Eq. (11))	(Eq. (11))	(Eq. (11))
Rolling stiffness	$k_r$	(Eq. (2))	(Eq. (2))	(Eq. (2))	(Eq. (2))
Local damping	(-)	0.7	0.7	0.7	0.7
Ball density	$\rho(\frac{\text{kg}}{\text{m}^3})$	2500	2500	2500	2500
Ball scaling factor	(-)	1	1	1	1
Confining pressures	$P(\text{kPa})$	• 100 • 300	• 100 • 300	• 100 • 200 • 300	• 100 • 200 • 300
Inertial number	$I(10^{-4})$	4.00	4.74	3.67	6.28

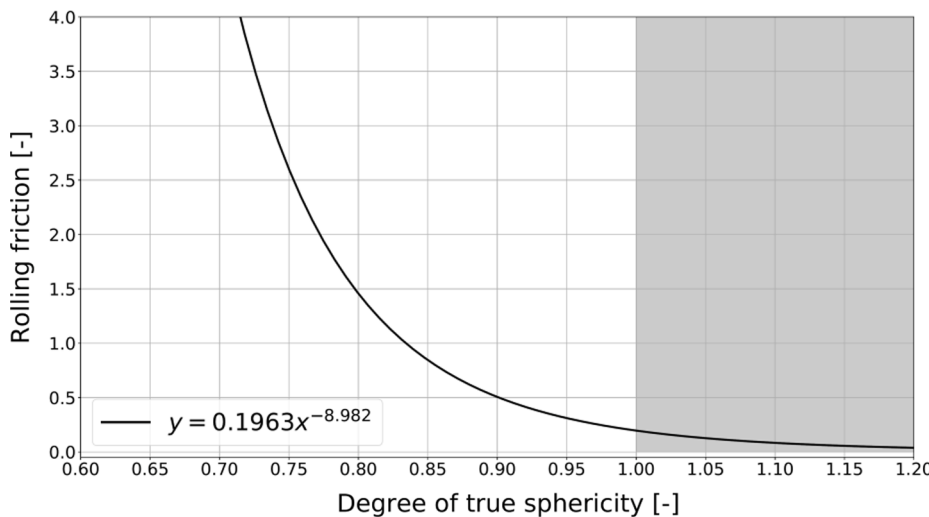


**Fig. 9.** Calibrated matching function between particle true sphericity and rolling friction coefficient. The shaded area indicates the inadmissible values of true sphericity.

#### 4. Model validations

##### 4.1. Further tests on Hostun and Caicos sands

The experimental dataset used for calibration was part of a larger triaxial testing campaign, as described by (Andò, 2013). That campaign included other triaxial tests on dense Hostun and Caicos specimens at higher confining pressures (300 kPa). Such tests offered a first suitable target for validation.

Numerical specimens identical to those described before were created, trying to approximate the initial porosities (before shearing) of the physical specimens as much as possible (Table 3). The specimens were compressed isotropically to 300 kPa and then sheared in triaxial condition until failure was attained. For each sand, all contact properties remain the same as in the 100 kPa confining case. The mapping function applied to assign rolling resistance to the elements is also the same.

Figs. 11 and 12 show the stress–strain–volumetric response of the numerical and experimental tests. The numerical curves compare well with the experiments, except for the volumetric dilation of the Caicos

specimen, which is again overestimated. This may be partly due to the boundary effects induced by the rigid lateral wall on the post-localization response. Another effect at play may be breakage and/or particle abrasion at this higher stress level. Even small amounts of particle breakage can have a significant effect on dilatancy (Ciantia et al., 2019b).

##### 4.2. Triaxial test on Ottawa sand

The experimental campaign by Andò (2013) also included tests in a different silica sand: Ottawa 50/70, which is also a material frequently used in geotechnical research (Table 1). The tests performed at 100 kPa (OUEA04) and 300 kPa (OUEA02) were selected for validation. The physical specimen OUEA04 had been scanned using the same tomographic procedures applied for the case of Hostun and Caicos, therefore 3D grain images are available. True sphericity values were computed for all the grains in the specimen (110.000), obtaining the distribution illustrated in Fig. 13. The sphericity values of Ottawa peak between those of Caicos and Hostun.

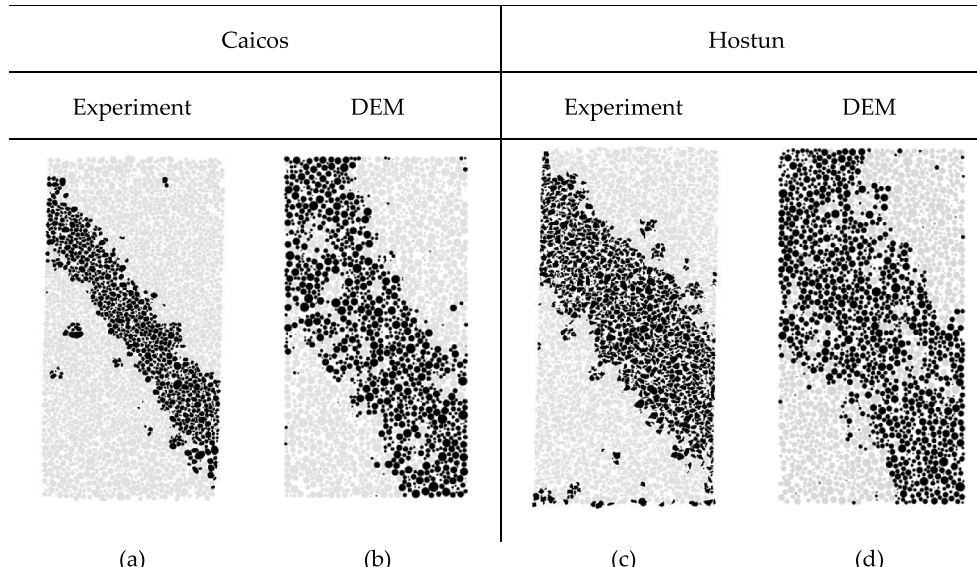


**Fig. 10.** Shear band identification for the experiments and the DEM simulation for both sands (specimens HNEA01 and COEA04). Physical (a-c) and numerical (b-d) particles are coloured black if they belong to the shear band. The same threshold separates the grains from both sands and both physical and numerical samples.

**Table 3**

Drained triaxial compression tests performed in this study. The relative density and porosity of each experimental/numerical test are reported. The symbol (\*) means that a denser specimen could not be generated for the DEM simulation.

Sand	Specimen	Relative density (EXP)	Confining pressure (kPa)	Initial porosity (EXP)	Initial porosity (DEM)
-	-	$D_R$ (%)	(kPa)	$n_{0,exp}$ (%)	$n_{0,DEM}$ (%)
Hostun	HNEA01	83	100	39.7	39.0
Hostun	HNEA02	95	300	38.2	38.6
Caicos	COEA04	-	100	31.9	33.2 (*)
Caicos	COEA02	-	300	33.2	34.3 (*)
Ottawa	OUEA04	112	100	31.4	34.1 (*)
Ticino	TC1	47	109	43.5	44.1
Ticino	TC2	46	200	43.7	43.0
Ticino	TC3	41	300	44.1	43.8
Ticino	TC4	72	100	40.5	39.8
Ticino	TC5	74	200	40.3	39.7
Ticino	TC6	75	300	40.1	40.2
Ticino	TC7	90	100	38.2	38.2
Ticino	TC8	93	200	37.8	38.4
Ticino	TC9	93	300	37.8	37.6

The DEM specimens were then prepared matching the experimental PSD and approximating as much as possible the initial porosity (Table 3). The specimens were prepared without scaling, including about 102.000 spherical elements, slightly below the number of grains contained in the physical sample. Specimen preparation and triaxial testing followed identical procedures as those previously described.

In principle, only the contact parameters  $E_{mod}$  and  $k_{ratio}$  (*i.e.*,  $k_n$  and  $k_s$ ) and coefficient of sliding friction ( $\mu$ ) were free to adjust, as the sphericity to rolling resistance mapping function applied was the same. In practice only  $E_{mod}$  and  $\mu$  were adjusted – using the test at 100 kPa – to values of 0.15 GPa and 0.45, respectively. The  $k_{ratio}$  value was maintained as 2.0, as in the other sands (Table 2).

Figs. 14 and 15 show the comparison between the experimental and

numerical results at 100 kPa and 300 kPa confinement, respectively. The figures include two experimental replicas of the tests, which were also available (OUEA06 and OUEA03, respectively for the 100 kPa and 300 kPa confinements). The simulations provide a good fit to the experiments; in this case even the post-localization volumetric mismatch is small.

#### 4.3. Triaxial tests on Ticino sand

Ticino sand (Table 1) is a poorly graded medium-sized sand, with grains of medium angularity. The macroscopic responses of Ticino sand have been well reproduced using DEM by several researchers either using clumps (Gotteland et al., 2009) or by inhibiting rotations (Calvetti 2008, Arroyo et al., 2011, Butlanska et al., 2014). Ticino sand will be here modelled using the rolling resistance model with rolling resistance values assigned through the mapping function (Eq. (11)).

There were no 3D tomographic images of Ticino sand readily available to establish the sphericity distribution to be input in the mapping function. As an alternative, a table scanner (*CanoScan LiDE 25*) was employed to acquire 2D images of about 4000 grains of Ticino sand. Rorato et al. (2019a) showed that this sample size is enough to obtain a good definition of the sphericity statistics. The table scanner used had 1200 dpi, or equivalently about 20  $\mu\text{m}/\text{pixel}$ , which is only slightly above the 15  $\mu\text{m}$  voxel side used in the 3D  $\mu\text{-CT}$  image acquisition for the other sands. The parallel projection of each grain on the scan surface avoids parallax errors. The scanned image was binarised, segmented and labelled using the open-source python package SPAM ()(Andò et al., 2017), as shown in Fig. 16.

Using a dedicated python script 2D perimeter sphericity was calculated for each grain identified in the image. Eq. (8) relating the known 2D perimeter sphericity ( $S_p$ ) and the 3D true sphericity ( $\psi$ ) was applied to obtain a statistical distribution of 3D true sphericity. This is plotted in Fig. 13: as for Ottawa sand, the mean sphericity of Ticino sand was located between those of Hostun and Caicos sands. It can be noted that

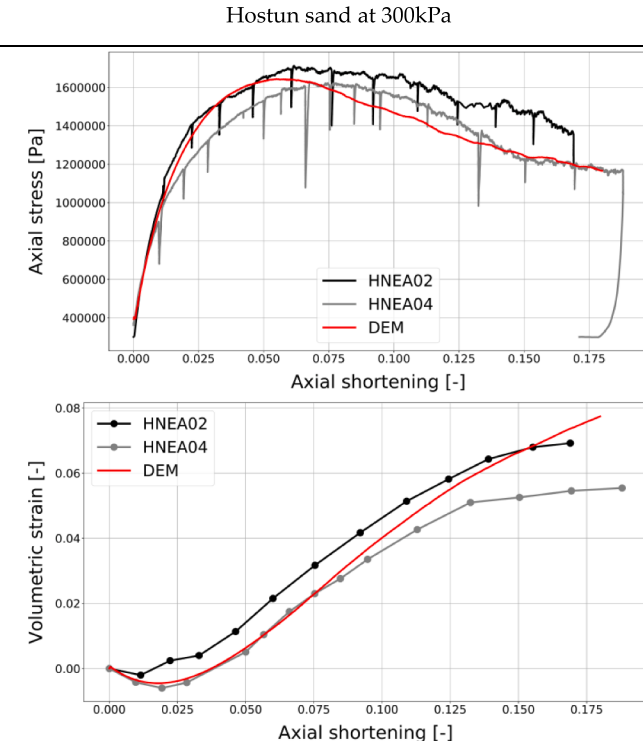
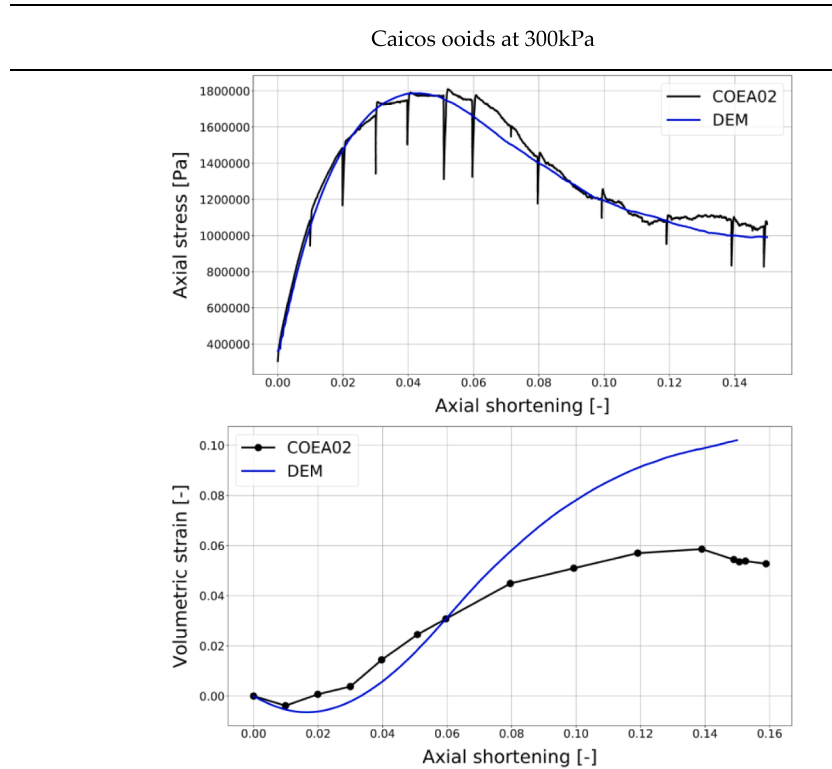


Fig. 11. Comparison between the triaxial responses (300 kPa confining pressure) of the experiments (specimens HNEA02 and HNEA04) and the numerical model (DEM) replicating Hostun sand.



**Fig. 12.** Comparison between the triaxial responses (300 kPa confining pressure) of the experiment (specimen COEA02) and the numerical model (DEM) replicating Caicos ooids.

the dispersion is higher than for the other sands, with a wide tail of low sphericities. This is likely a side effect of the approximations involved in the 2D procedure.

DEM triaxial simulations were carried out for a total of nine triaxial tests, including specimens at dense ( $D_R \cong 90\%$ ), medium ( $D_R \cong 75\%$ ) and loose ( $D_R \cong 50\%$ ) states, at variable confining pressures (100, 200 and 300 kPa). The triaxial chamber used for the DEM simulations kept the same geometry as that employed for Caicos, Hostun and Ottawa (Table 2), which – in this case – was much smaller than that employed in the physical experiments. Again, no particle scaling was applied and, due to the larger grain size of Ticino sand, about 16,000 elements were employed in each numerical specimen.

One specimen (100 kPa confining,  $D_R \cong 75\%$ ) was selected to calibrate contact parameters  $E_{mod}$  and  $\mu$  (the  $k_{ratio}$  value was kept at 2, as in the other sands). After a few iterations the values finally selected were, respectively, 0.4 GPa and 0.60 (Table 2).

The mechanical responses (stress–strain–volumetric) of the nine DEM

simulations are shown alongside the corresponding experimental results in Fig. 17 ( $D_R \cong 50\%$ ), Fig. 18 ( $D_R \cong 75\%$ ) and Fig. 19 ( $D_R \cong 90\%$ ). It is evident that the triaxial response is well reproduced under all stress and state conditions used in the tests. Small discrepancies can be seen for the DEM simulations at 300 kPa but it must be mentioned that some particle crushing - not modelled here - was noted in the physical samples at the end of those tests.

This case strongly suggests that there is no need to have a full three-dimensional tomographic identification of sand grain shapes. Thanks to the good correlation between true sphericity and 2D perimeter sphericity (equation (8)), the required rolling resistance for DEM analysis can be readily determined based on the observations of 2D images.

## 5. Discussion

A comparison can be made with the approach proposed by Wensrich and Katterfeld (2012), who, based on geometric deductive reasoning, suggested that rolling resistance could be evaluated as the ratio of grain surface – averaged contact eccentricity  $\langle e \rangle$  and the equivalent grain radius (*i.e.*, the radius of a sphere with equal volume as the grain),  $R_{eq}$

$$\mu_r = \frac{\langle e \rangle}{R_{eq}} \quad (12)$$

The rolling friction values evaluated with Eq. (12) are compared with those predicted by Eq. (11) in Fig. 20. The rolling friction values obtained are similar for high sphericity values. Despite this coincidence, it is noted that further work with the average contact eccentricity concept (Wensrich et al., 2014) concluded that values given by Eq. (12), should be halved to obtain good matches with clump-based simulations, which would separate further the eccentricity-based rolling friction values from those derived from our proposal. This difference may reflect the decision to represent in our model not just structural rolling resistance - *i.e.*, the one reflected by eccentricity - but also contact-level sources or

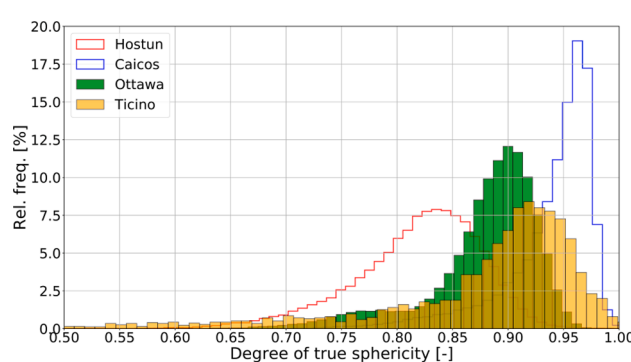


**Fig. 13.** Statistical distributions of 3D true sphericity for Hostun, Caicos, Ottawa and Ticino sands.

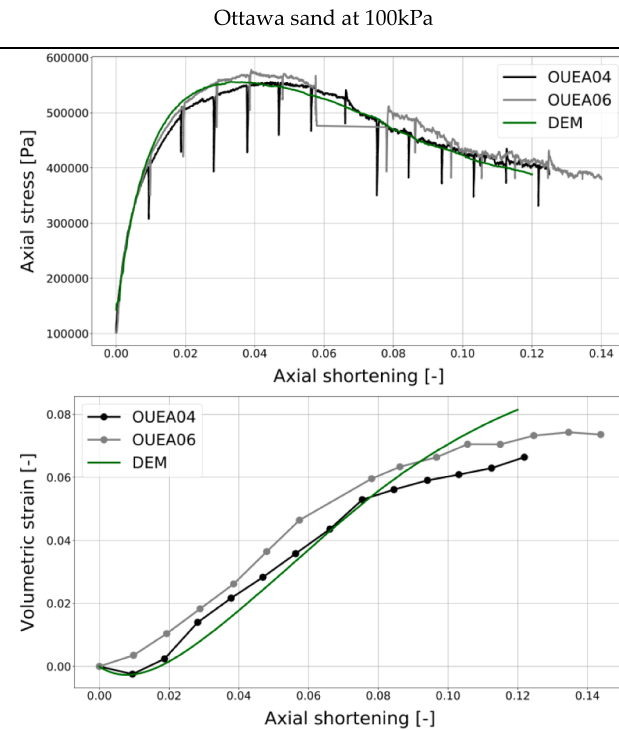


**Fig. 14.** Comparison between the triaxial responses (100 kPa confining pressure) of the experiments (specimens OUEA04 and OUEA06) and the numerical model (DEM) replicating Ottawa sand.

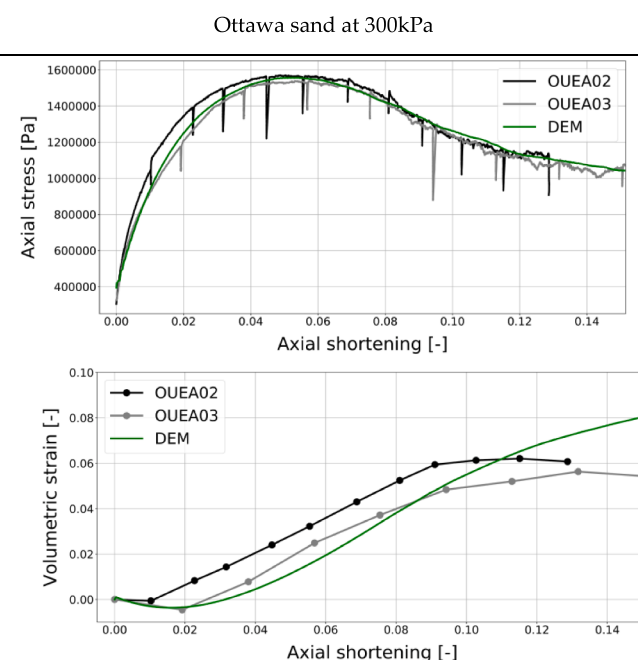


**Fig. 15.** Comparison between the triaxial responses (300 kPa confining pressure) of the experiments (specimens OUEA02 and OUEA03) and the numerical model (DEM) replicating Ottawa sand.

rolling resistance, allowing non-zero rolling resistance for spheres.

Another interesting comparison is with the work of Kawamoto (Kawamoto et al., 2018) who built a DEM-based “avatar” of specimen of HNEA01 in which a much higher level of detail of each grain shape was represented, via level sets. The “avatar” approach does not individuate single grains for validation, but, as done here with average shear band

rotation, relies on emerging ensemble measures (like shear band orientation) for validation. The simulation results obtained by Kawamoto et al. (2018) for Hostun using a level set method to incorporate explicitly grain shape are also included in Fig. 6 for comparison. The results are not very different from those obtained here, with discrepancies in dilatancy attributable to the much more realistic numerical

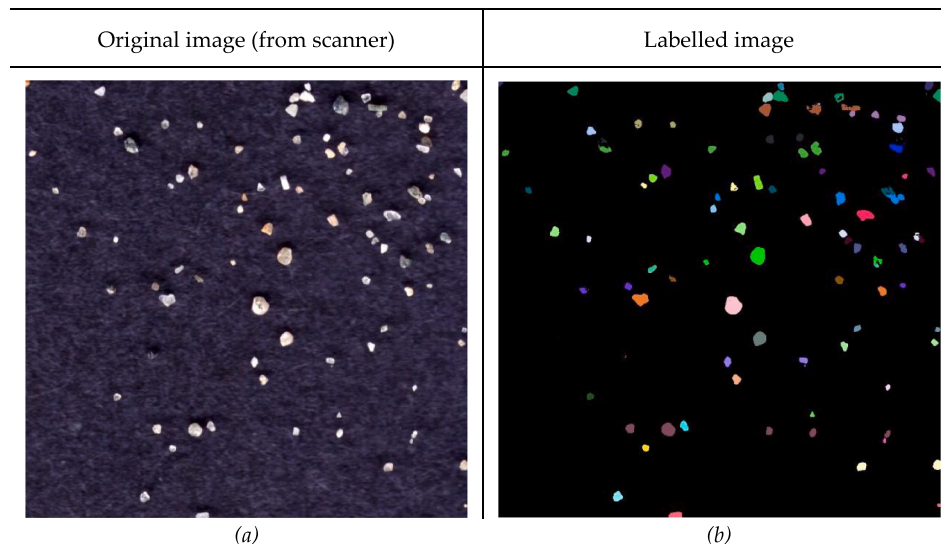


**Fig. 16.** Zoom on (a) the original scan and (b) the labelled image of Ticino sand.

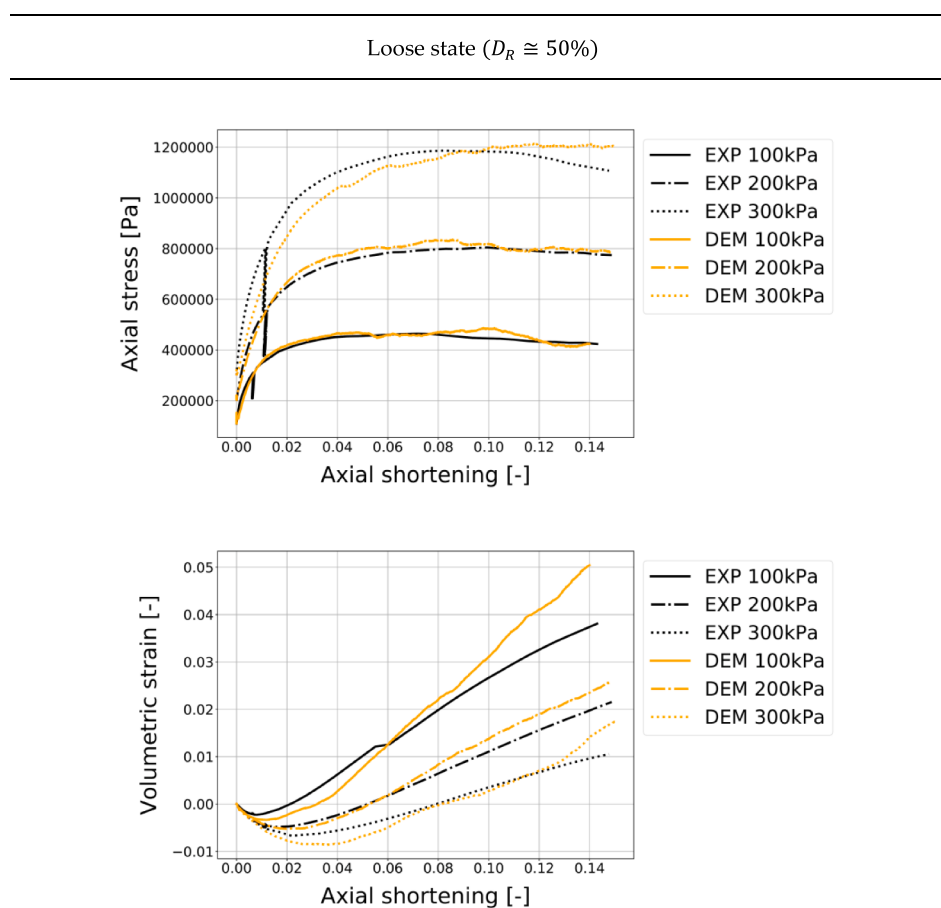


**Fig. 17.** Triaxial responses of loose Ticino sand at 100–200–300 kPa.

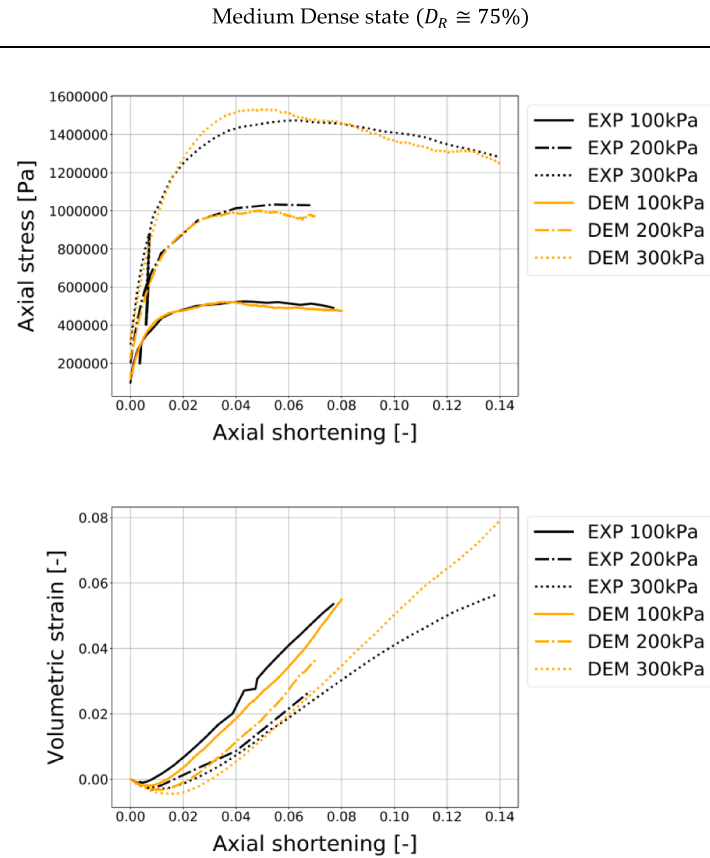
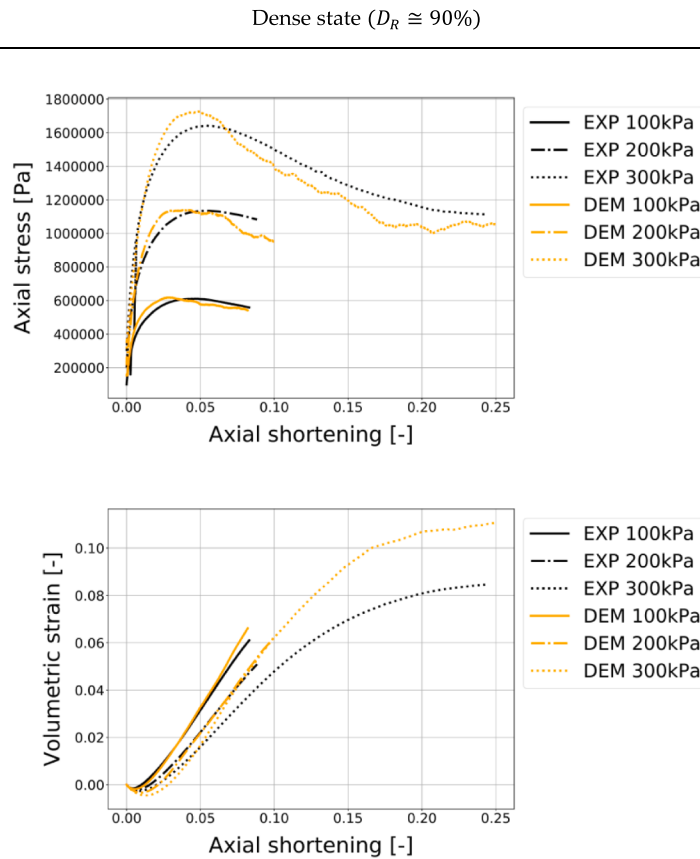
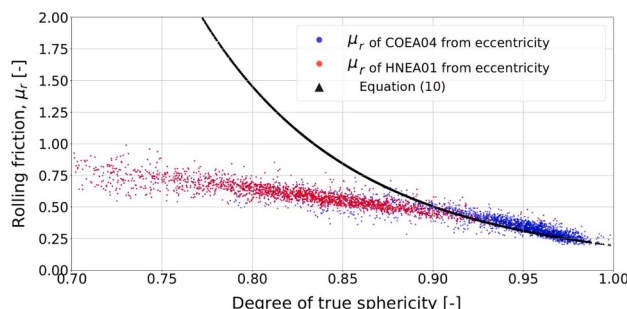


Fig. 18. Triaxial responses of medium Ticino sand at 100–200–300 kPa.



**Fig. 19.** Triaxial responses of dense Ticino sand at 100–200–300 kPa.



**Fig. 20.** Comparison of rolling friction values derived from average eccentricity following Wensrich and Katterfeld (2012) and those given by the calibrated mapping function.

representation of boundary conditions (loading platens and flexible membrane surrounding the specimen) in the work of Kawamoto et al. (2018). It is also interesting that the sliding friction value that was calibrated (0.575) by Kawamoto et al. (2018) was very close to the one calibrated here (0.55). Of course, the computational cost is very different: while simulating specimen HNEA01 through level set approach took 17 h in the 480 cores of the San Diego Supercomputer, using the model calibrated here a simulation of the same specimen lasts 20 h in a four-core desktop computer.

## 6. Conclusions

This paper presents a novel technique to relate univocally the degree of true sphericity of each grain contained in a sand sample with the

coefficient of rolling friction to apply to its numerical counterpart of spherical shape. This approach greatly simplifies the complex calibration procedure of rolling resistance contact models, easily incorporating information on natural shape variability in the numerical discrete model.

It has been also shown that easily-acquired 2D proxy measures of sphericity can be used instead of the more difficult to acquire direct 3D measurements. A relatively cheap table scanner may be all that is required to evaluate the coefficient of rolling friction.

For the four different sands examined, the approach appeared to work successfully using a unique mapping function between true sphericity and rolling friction. However, the validity of the approach has only been tested for triaxial compression paths. With different stress paths seems necessary in this respect. Future work will also explore if the proposed mapping of sphericity into rolling friction holds true when other modelling features are modified, such as the allocation rule for rolling friction at the contact, or the definition of contact stiffness (e.g. by using a Hertzian contact model instead of linear stiffness).

## CRediT authorship contribution statement

**R. Rorato:** Methodology, Investigation, Formal analysis, Writing - original draft. **M. Arroyo:** Writing - review & editing, Project administration, Funding acquisition. **A. Gens:** Investigation, Software, Writing - review & editing. **E. Andò:** Supervision, Funding acquisition, Writing - review & editing. **G. Viggiani:** Supervision, Writing - review & editing.

## Declaration of Competing Interest

The authors declare that they have no known competing financial interests or personal relationships that could have appeared to influence

the work reported in this paper.

## Acknowledgments

The support of EU through 645665 - GEO-RAMP - MSCA-RISE and of the Ministry of Economy of Spain through research Grant BIA2014-59467-R is gratefully acknowledged. Laboratoire 3SR is part of the LabEx Tec 21 (Investissements d'Avenir - grant agreement n\_ANR-11-LABX-0030).

## References

- Ai, J., Chen, J.F., Rotter, J.M., Ooi, J.Y., 2011. Assessment of rolling resistance models in discrete element simulations. *Powder Technology*, 206(3): 269–282. Elsevier B.V. doi:10.1016/j.powtec.2010.09.030.
- Andò, E., 2013. *Experimental investigation of microstructural changes in deforming granular media using x-ray tomography*. PhD Thesis. Université de Grenoble.
- Andò, E., Cailletaud, R., Roubin, E., Stamati, O., and the spamp contributors. 2017. SPAMP: The Software for the Practical Analysis of Materials.
- Arroyo, M., Butlanska, J., Gens, A., Calvetti, F., Jamiolkowski, M., 2011. Cone penetration tests in a virtual calibration chamber. *Geotechnique* 61 (6), 525–531. <https://doi.org/10.1680/geot.9.P.067>.
- Bardet, J.P., 1994. Observations on the effects of particle rotations on the failure of idealized granular materials. *Mech. Mater.* 18 (2), 159–182.
- Belheine, N., Plassiard, J.P., Donzé, F.V., Darve, F., Seridi, A., 2009. Numerical simulation of drained triaxial test using 3D discrete element modeling. *Comput. Geotech.* 36 (1–2), 320–331. <https://doi.org/10.1016/j.compgeo.2008.02.003>.
- Boon, C.W., Housler, G.T., Utili, S., 2012. A new algorithm for contact detection between convex polygonal and polyhedral particles in the discrete element method. *Comput. Geotech.* 44, 73–82.
- Butlanska, J., Arroyo, M., Gens, A., O'Sullivan, C., 2014. Multi-scale analysis of cone penetration test (CPT) in a virtual calibration chamber. *Can. Geotech. J.* 51 (1), 51–66. <https://doi.org/10.1139/cgj-2012-0476>.
- Butlanska, J., 2014. Cone penetration test in a virtual calibration chamber (Doctoral dissertation. Universitat Politècnica de Catalunya (UPC)).
- Butlanska, J., Arroyo, M., Amoroso, S., Gens, A., 2018. Marchetti flat dilatometer tests in a virtual calibration chamber. *Geotech. Test. J.* 41 (5), 930–945. <https://doi.org/10.1520/GTJ20170370>.
- Calvetti, F., 2008. Discrete modelling of granular materials and geotechnical problems. *Eur. J. Environ. Civil Eng.* 12 (7–8), 951–965. <https://doi.org/10.3166/EJCE.12.951-965>.
- Calvetti, F., Viggiani, G., and Tamagnini, C. 2003. A numerical investigation of the incremental behavior of granular soils. *Rivista Italiana di Geotecnica*, 37(3): 11–29. Available from: [http://www.associazionegiotechnica.it/sites/default/files/rig/RIG\\_2003\\_3.11.pdf](http://www.associazionegiotechnica.it/sites/default/files/rig/RIG_2003_3.11.pdf).
- Catalano, E., Chareyre, B., Barthélémy, E., 2014. Pore-scale modeling of fluid-particles interaction and emerging poromechanical effects. *Int. J. Numer. Anal. Methods Geomech.*, 38(1): 51–71. John Wiley and Sons, Ltd. doi:10.1002/nag.2198.
- Cheng, H., Shuku, T., Thoeni, K., Yamamoto, H., 2018. Probabilistic calibration of discrete element simulations using the sequential quasi-Monte Carlo filter. *Granular Matter* 20 (1), 11.
- Cheng, K., Wang, Y., Yang, Q., Mo, Y., Guo, Y., 2017. Determination of microscopic parameters of quartz sand through tri-axial test using the discrete element method. *Comput. Geotech.*, 92(August): 22–40. Elsevier Ltd. doi:10.1016/j.compgeo.2017.07.017.
- Ciantia, M.O., Arroyo, M., Calvetti, F., Gens, A., 2015. An approach to enhance efficiency of DEM modelling of soils with crushable grains. *Geotechnique* 65 (2), 91–110. <https://doi.org/10.1680/geot.13.P.218>.
- Ciantia, M.O., Arroyo, M., O'Sullivan, C., Gens, A., Liu, T., 2019a. Grading evolution and critical state in a discrete numerical model of Fontainebleau sand. *Geotechnique*, 69 (1): 1–15. Thomas Telford Ltd. doi:10.1680/geot.17.P.023.
- Ciantia, M.O., Arroyo, M., O'Sullivan, C., Gens, A., 2019. Micromechanical inspection of incremental behaviour of crushable soils. *Acta Geotech.* 14 (5), 1337–1356.
- Combe, A.-L., 1998. Comportement du sable d'Hostun S28 au triaxial axisymétrique. Université Joseph Fourier, Grenoble, Comparaison avec le sable d'Hostun RF.
- Cundall, P.A., Strack, O.D.L., 1979. A discrete numerical model for granular assemblies. *Geotechnique* 29 (1), 47–65. <https://doi.org/10.1680/geot.1979.29.1.47>.
- Cho, A.G., Dodds, J., Santamarina, J.C., 2006. Particle shape effects on packing density, stiffness and strength – natural and crushed sands. *J. Geotech. Geoenviron. Eng.* 132 (5), 591–602. [https://doi.org/10.1061/\(ASCE\)1090-0241\(2006\)132:5\(591\)](https://doi.org/10.1061/(ASCE)1090-0241(2006)132:5(591)).
- Da Cruz, F., Emam, S., Prochnow, M., Roux, J.N., Chevoir, F., 2005. Rheophysics of dense granular materials: Discrete simulation of plane shear flows. *Phys. Rev. E - Statistical, Nonlinear, Soft Matter Phys.* 72 (2), 1–17. <https://doi.org/10.1103/PhysRevE.72.021309>.
- Estrada, N., Taboada, A., Radjaï, F., 2008. Shear strength and force transmission in granular media with rolling resistance. *Phys. Rev. E - Statistical, Nonlinear, and Soft Matter Phys.* 78 (2), 1–11. <https://doi.org/10.1103/PhysRevE.78.021301>.
- Feng, Y.T., Owen, D.R.J., 2014. Discrete element modelling of large scale particle systems—I: exact scaling laws. *Comput. Particle Mech.* 1 (2), 159–168.
- Gotteland, P., Villard, P., Salot, C., Nakagawa, M., Luding, S., 2009. Using nonconvex discrete elements to predict experimental behaviour of granular materials. In: Proceedings of the 6th International Conference on Micromechanics of Granular Media. AIP, pp. 361–364. <https://doi.org/10.1063/1.3179934>.
- Hall, S.A., Bornert, M., Desrues, J., Pannier, Y., Lenoir, N., Viggiani, G., Bésuelle, P., 2010. Discrete and continuum analysis of localised deformation in sand using X-ray µCT and volumetric digital image correlation. *Géotechnique*, 60 (5), 315–322.
- Hosn, R.A., Sibille, L., Benahmed, N., Chareyre, B., 2018. A discrete numerical model involving partial fluid-solid coupling to describe suffusion effects in soils. *Comput. Geotech.* 95, 30–39.
- Huang, X., Hanley, K.J., O'Sullivan, C., Kwok, C.Y., 2017. Implementation of rotational resistance models: a critical appraisal. *Particuology* 34, 14–23.
- Itasca Consulting Group Inc., 2014. PFC — Particle Flow Code, Ver. 5.0. Minneapolis: Itasca. Available from: <https://www.itascacg.com/software-faq>.
- Irazábal, J., Salazar, F., Onate, E., 2017. Numerical modelling of granular materials with spherical discrete particles and the bounded rolling friction model. Application to railway ballast. *Comput. Geotech.* 85, 220–229.
- Iwashita, K., Oda, M., 1998. Rolling resistance at contacts in simulation of shear band development by DEM. *J. Eng. Mech.* 124 (3), 285–292. [https://doi.org/10.1061/\(ASCE\)0733-9399\(1998\)124:3\(285\)](https://doi.org/10.1061/(ASCE)0733-9399(1998)124:3(285)).
- Iwashita, K., Oda, M., 2000. Micro-deformation mechanism of shear banding process based on modified distinct element method. *Powder Technol.* 109 (1–3), 192–205. [https://doi.org/10.1016/S0032-5910\(99\)00236-3](https://doi.org/10.1016/S0032-5910(99)00236-3).
- Jamiolkowski, M., Lo Presti, D.C.F., Manassero, M., 2003. Evaluation of Relative Density and Shear Strength of Sands from CPT and DMT. In: Symposium on Soil Behavior and Soft Ground Construction Honoring Charles C. "Chuck" Ladd. Cambridge, USA. doi:10.1061/40659(2003)7.
- Jerves, A.X., Kawamoto, R.Y., Andrade, J.E., 2016. Effects of grain morphology on critical state: A computational analysis. *Acta Geotech.* 11 (3), 493–503. <https://doi.org/10.1007/s11440-015-0422-8>.
- Jiang, M.J.J., Yu, H.-S., Harris, D., 2005. A novel discrete model for granular material incorporating rolling resistance. *Comput. Geotech.* 32 (5), 340–357. <https://doi.org/10.1016/j.compgeo.2005.05.001>.
- Katagiri, J., Matsushima, T., Yamada, Y., Katagiri, J., Matsushima, T., Yamada, Y., 2010. Simple shear simulation of 3D irregularly-shaped particles by image-based DEM. *Granular Matter* 12, 491–497. <https://doi.org/10.1007/s10035-010-0207-6>.
- Kawamoto, R., Andò, E., Viggiani, G., Andrade, J.E., 2018. All you need is shape: Predicting shear banding in sand with LS-DEM. *J. Mech. Phys. Solids*, 111: 375–392. Elsevier Ltd. doi:10.1016/j.jmps.2017.10.003.
- Kawano, K., Shire, T., O'Sullivan, C., 2018. Coupled particle-fluid simulations of the initiation of suffusion. *Soils Found.* 58 (4), 972–985.
- Khoubani, A., Evans, T.M., 2018. An efficient flexible membrane boundary condition for DEM simulation of axisymmetric element tests. *Int. J. Numer. Anal. Meth. Geomech.* 42 (4), 694–715.
- Lee, J.-S., Dodds, J., Santamarina, J.C., 2007. Behavior of rigid-soft particle mixtures. *J. Mater. Civ. Eng.* 19 (2), 179–184. [https://doi.org/10.1061/\(ASCE\)0899-1561\(2007\)19](https://doi.org/10.1061/(ASCE)0899-1561(2007)19).
- Li, T., Jiang, M., Thornton, C., 2018. Three-dimensional discrete element analysis of triaxial tests and wetting tests on unsaturated compacted silt. *Comput. Geotech.* 97, 90–102.
- Lin, X., Ng, T.T., 1997. A three-dimensional discrete element model using arrays of ellipsoids. *Geotechnique* 47 (2), 319–329.
- Liu, Q.B., Lehane, B.M., 2013. The influence of particle shape on the (centrifuge) cone penetration test (CPT) end resistance in uniformly graded granular soils. *Géotechnique* 60 (2), 111–121. <https://doi.org/10.1139/t06-037>.
- Lu, M., McDowell, G.R., 2007. The importance of modelling ballast particle shape in the discrete element method. *Granular Matter* 9 (1–2), 69–80. <https://doi.org/10.1007/s10035-006-0021-3>.
- Lu, G., Third, J.R., Müller, C.R., 2015. Discrete element models for non-spherical particle systems: from theoretical developments to applications. *Chem. Eng. Sci.* 127, 425–465.
- Matsushima, 2002. Discrete Element Modeling for Irregularly-Shaped Sand Grains. La Modélisation aux Éléments Discrets d'un sable à grains de forme irrégulière (1998): 239–246.
- Mohamed, A., Gutierrez, M., 2010. Comprehensive study of the effects of rolling resistance on the stress-strain and strain localization behavior of granular materials. *Granular Matter* 12 (5), 527–541.
- Rorato, R., Arroyo, M., Andò, E., Gens, A., Viggiani, G., 2020. Linking shape and rotation of grains during triaxial compression of sand, under review. *Granular Matter*.
- Rorato, R., Arroyo, M., Andò, E., Gens, A., 2019. Sphericity measures of sand grains. *Eng. Geol.* 254 (4), 43–53.
- Rorato, R., 2019. Imaging and discrete modelling of sand shape. PhD Thesis. Universitat Politècnica de Catalunya (UPC).
- Rorato, R., Arroyo, M., Gens, A., Andò, E., Viggiani, G., 2018. Particle Shape Distribution Effects on the Triaxial Response of Sands: A DEM Study. In: micro to MACRO Mathematical Modelling in Soil Mechanics, Trends in Mathematics. Edited by P. Giovine and et al., Reggio Calabria (Italy). pp. 277–286. doi:10.1007/978-3-319-99474-1-28.
- Rothenburg, L., Bathurst, R.J., 1992. Micromechanical features of granular assemblies with planar elliptical particles. *Géotechnique* 42 (1), 79–95.
- Sakaguchi, H., Ozaki, E., Igarashi, T., 1993. Plugging of the flow of granular materials during the discharge from a silo. *Int. J. Mod. Phys. B* (09–10), 1949–1963. <https://doi.org/10.1142/S0217979293002705>.
- Vaid, Y., Chern, J., Tumi, H., 1985. Confining pressure, grain angularity and liquefaction. *J. Geotech. Eng.* 111 (10), 1229–1235.
- Wadell, H., 1932. Volume, Shape, and Roundness of Rock Particles. *J. Geol.* 40 (5), 443–451.

- Wensrich, C.M., Katterfeld, A., 2012. Rolling friction as a technique for modelling particle shape in DEM. *Powder Technology*, 217: 409–417. Elsevier B.V. doi: 10.1016/j.powtec.2011.10.057.
- Wensrich, C.M., Katterfeld, A., Sugo, D., 2014. Characterisation of the effects of particle shape using a normalised contact eccentricity. *Granular Matter* 16 (3), 327–337. <https://doi.org/10.1007/s10035-013-0465-1>.
- Williams, J.R., Pentland, A.P., 1992. Superquadrics and modal dynamics for discrete elements in interactive design. *Eng. Comput.* 9 (2), 115–127.
- Xiao, Y., Long, L., Matthew Evans, T., Zhou, H., Liu, H., Stuedlein, A.W., 2019. Effect of particle shape on stress-dilatancy responses of medium-dense sands. *J. Geotech. Geoenviron. Eng.* 145 (2) [https://doi.org/10.1061/\(ASCE\)GT.1943-5606.0001994](https://doi.org/10.1061/(ASCE)GT.1943-5606.0001994).
- Yang, J., Luo, X.D., 2015. Exploring the relationship between critical state and particle shape for granular materials. *J. Mech. Phys. Solids* 84, 196–213. <https://doi.org/10.1016/j.jmps.2015.08.001>.
- Zhang, N., Arroyo, M., Ciantia, M.O., Gens, A., Butlanska, J., 2019. Standard penetration testing in a virtual calibration chamber. *Comput. Geotech.* 111, 277–289.
- Zhang, N., Evans, T.M., 2019. Discrete numerical simulations of torpedo anchor installation in granular soils. *Comput. Geotech.* 108, 40–52.
- Zhao, D., Nezami, E.G., Hashash, Y.M., Ghaboussi, J., 2006. Three-dimensional discrete element simulation for granular materials. *Eng. Comput.* 23 (7), 749–770.
- Zhao, S., Evans, T., Zhou, X., 2018. Effects of curvature-related DEM contact model on the macro-and micro-mechanical behaviours of granular soils. *Géotechnique* 17 (158), 21.
- Zhou, B., Huang, R., Wang, H., Wang, J., 2013. DEM investigation of particle anti-rotation effects on the micromechanical response of granular materials. *Granular Matter* 15 (3), 315–326. <https://doi.org/10.1007/s10035-013-0409-9>.